NANO · MICRO small
www.small-journal.com

A Powerful Tumor Catalytic Therapy by an Enzyme-Nanozyme Cascade Catalysis (ENCAT) System

*Min Zhou, Jiayuan Feng, Qi Mei, Tong Li, Yihong Zhang, Wanling Liu, and Hui Wei**

Complexity of tumor and its microenvironment as obstacles often restrict traditional tumor therapies. Enzyme/nanozyme-mediated catalytic therapy has been emerged, but the efficacy of single catalytic therapy is still moderate. Inspired by the concepts of catalytic and synergetic therapy, an enzyme-nanozyme cascade catalysis (ENCAT)-enhanced tumor therapy is developed. First, metal–organic framework (MOF) PCN222-Mn (PM) and glucose oxidase (GOx) are chosen as nanozyme and natural enzyme, respectively. Then two assembled together to form enzyme-nanozyme complex PCN222-Mn@GOx (PMG). To achieve tumor targeting and GOx protection, hyaluronic acid (HA) is modified on PMG to obtain PCN222-Mn@GOx/HA (PMGH). Both cellular and animal studies demonstrate a cascade catalysis-enhanced tumor therapy by PMGH. Specifically, a cascade catalysis-enhanced PDT is achieved based on enzyme-nanozyme mediated cascade-catalyzed O_2 generation; an enhanced synergistic therapy is demonstrated by combining PM-mediated PDT, GOx-mediated starvation therapy, and activated/promoted immunotherapy together. Additionally, the designed tumor catalytic therapy is explored in a tumor bearing mouse model, where it exhibits powerful anti-tumor effects against both primary and metastatic tumors. This strategy has the potential to broaden tumor therapeutic approaches.

1. Introduction

Tumors and their microenvironments are characterized by hypoxia, elevated hydrogen peroxide (H_2O_2) and glutathione (GSH), and glucose addiction.[1–4] Unfortunately, these features pose insurmountable barriers to cancer therapies, including hypoxia-limited photodynamic therapy (PDT), GSH-weakened reactive oxygen species (ROS)-mediated therapy, and glucose addiction-hampered immunotherapy.[5–10] Encouragingly, emerging catalytic strategies have shown promise to enhance these therapies, such as catalase (CAT)-mediated hypoxic relief-enhanced PDT and glucose oxidase (GOx)-mediated glucose consumption-promoted immunotherapy.[11–14] However, due to the non-targeting and easy deactivation of natural enzymes, developing efficient delivery or highly stable enzyme alternatives for natural enzymes is in demand.[15–18]

Nanozymes (nanomaterials with enzyme-like activity) are emerging alternatives to natural enzymes. They have superior properties including passive targeting ability, good stability, and broad reacting condition, showing promise for enhancing tumor therapy.[19–21] A series of nanozyme-mediated tumor therapies have been developed: peroxidase (POD)-like nanozymes can induce more toxic ROS by decomposing H_2O_2 into hydroxy radical ($^{\bullet}OH$);[22,23] CAT-like nanozymes can boost O_2-demanding PDT by catalyzing H_2O_2 for O_2 generation;[24–27] and GOx-like nanozymes can induce starvation therapy by consuming glucose.[28–32] However, there still have some limitations for nanozyme-mediated tumor therapies: POD-like nanozymes usually need to cooperate with inhibition of cellular antioxidants for optimal ROS generation; CAT-like nanozymes for enhanced PDT still need extra photosensitizers; and only "naked" Au NPs have moderate GOx-like activity.[19,33–35]

To address above limitations of catalytic therapies, here we developed an enzyme-nanozyme cascade catalysis (ENCAT)-enhanced tumor therapy. This strategy not only effectively surmounted limitations of single catalytic therapies but also achieved an enhanced tumor therapy. As shown in **Figure 1**, porphyrin-manganese (TCPP-Mn) was selected as a photosensitive ligand, coordinating with zirconium clusters to form metal–organic framework (MOF) PCN222-Mn (termed PM). PM not only mimicked CAT activity but also acted as a photosensitizer

---

M. Zhou, J. Feng, Q. Mei, T. Li, Y. Zhang, W. Liu, H. Wei
Department of Biomedical Engineering
College of Engineering and Applied Sciences
Nanjing National Laboratory of Microstructures
Jiangsu Key Laboratory of Artificial Functional Materials
Nanjing University
Nanjing, Jiangsu 210023, P. R. China
E-mail: weihui@nju.edu.cn

H. Wei
Nanozyme Laboratory in Zhongyuan
Henan Academy of Innovations in Medical Science
Zhengzhou, Henan 451163, P. R. China

H. Wei
State Key Laboratory of Analytical Chemistry for Life Science
School of Chemistry and Chemical Engineering
Chemistry and Biomedicine Innovation Center (ChemBIC)
ChemBioMed Interdisciplinary Research Centre at Nanjing University
Nanjing University
Nanjing, Jiangsu 210008, P. R. China

The ORCID identification number(s) for the author(s) of this article can be found under https://doi.org/10.1002/smll.202409363

DOI: 10.1002/smll.202409363

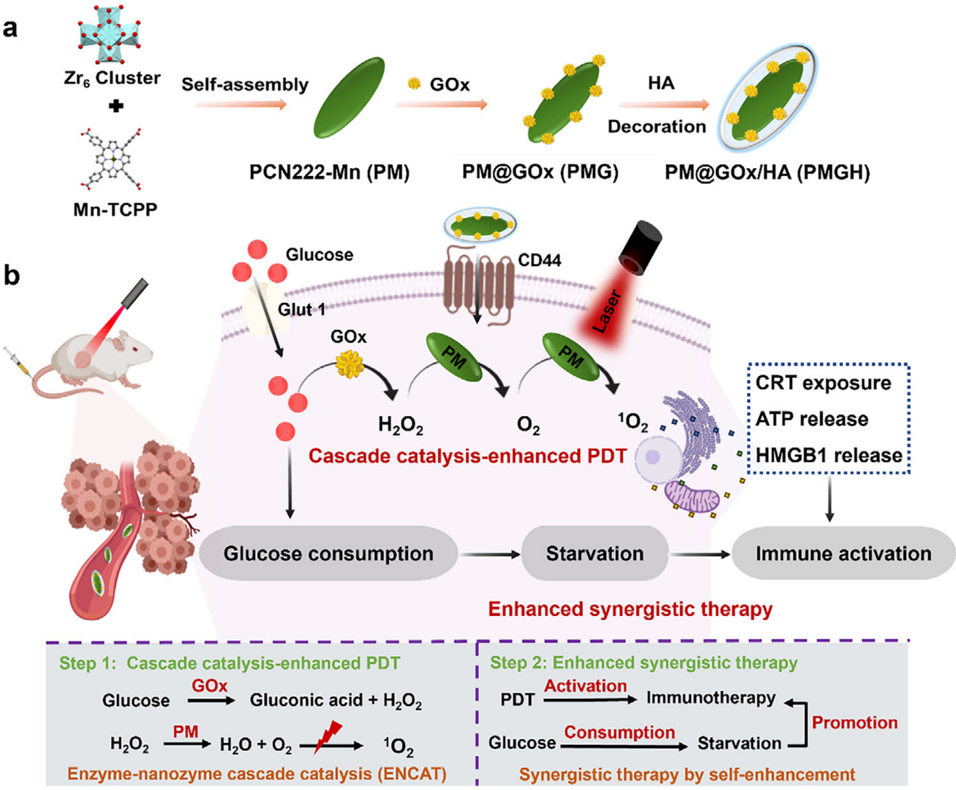

Figure 1. Scheme of enzyme-nanozyme cascade catalysis (ENCAT)-enhanced tumor therapy. a) Scheme of PCN222-Mn@GOx/HA (PMGH) synthesis. b) Processes of ENCAT-enhanced PDT and enhanced synergistic therapy.

for PDT. Subsequently, GOx as a natural enzyme was adsorbed on the surface of PM through electrostatic interactions to obtain PCN222-Mn@GOx (termed PMG). Then, hyaluronic acid (HA) as a targeting element was co-fabricated with GOx on the surface of PM to form PCN222-Mn@GOx/HA (termed PMGH). Upon PMGH injection, effective tumor accumulation was achieved through both active and passive targeting. After entering tumor cells, GOx consumed cellular glucose and generated H_2O_2. PM catalyzed both GOx-generated and endogenous H_2O_2 into O_2 for PDT enhancement. Furthermore, PDT-caused cell death induced immunotherapy, which was improved by GOx-mediated starvation therapy. In combination, our designed PMGH efficiently ablated primary tumors and distant metastasis for breast cancer based on the ENCAT-enhanced tumor therapy (Figure 1).

2. Results and Discussion

2.1. Preparation and Characterization of ENCAT System

TCPP-Mn, as the ligand of PM, was synthesized according to the previously reported methods.[36–39] Briefly, the mixture of [5,10,15,20-tetrakis (4-methoxycarbonylphenyl) porphyrin] and $MnCl_2{\cdot}4H_2O$ reacted to produce TCPP-Mn. The obtained TCPP-Mn was characterized by FTIR (Fourier transform infrared spectrometry) and HRMS (high resolution mass spectrometry) measurements (Figure S1, Supporting Information). Next, PM was synthesized by the reaction between TCPP-Mn, $ZrOCl_2{\cdot}8H_2O$, and benzoic acid as the previous reported method.[36–39] The formation of PM was confirmed by a transmission electron microscope (TEM). As shown in **Figure** 2a, uniform morphology of PM was demonstrated. Dynamic light scattering (DLS) analysis showed an average hydrodynamic diameter of 103.3 ± 1.3 nm (polydispersity index, PDI = 0.116) (Figure 2b) and a positive charge of 33.2 mV (Figure 2g). Based on the strong positive charge of PM and negative charge of GOx, GOx could be assembled on the surface of PM by electrostatic interaction. Different weight ratios (feed ratios) of PM:GOx, including 1:0.1, 1:0.2, and 1:0.5, were set for nanozyme and natural enzyme assembly. Different ratios of PM:GOx led to varying sizes and zeta potentials of PMG. The more GOx was used, the larger hydrodynamic diameter was observed, which could even result in aggregation (Figure 2c,d; Figures S2 and S3, Supporting Information). Hence, we chose the weight ratio of 1:0.1 for further PMG synthesis. HA, for its excellent active tumor targeting ability,[40,41] was employed for active targeting in our design. We chose the weight ratio (feed ratio) of HA with PMG as 5:1. The morphology of PMGH was similar to that of PMG (Figure 2e). Hydrodynamic diameter of PMGH was slightly smaller than that of PMG (Figure 2f), and zeta potential of PMGH was changed into negative one from positive PMG (Figure 2g). We attributed the charge reversal to the strongly negative HA, which could consolidate the electrostatic adsorption. Next, we checked the crystalline properties of PM, PMG, and PMGH using X-ray diffraction (XRD) (Figure 2h). Diffraction peaks of PM, PMG, and PMGH were consistent with the simulated PCN222-Mn. Ultraviolet-visible absorption spectra were also recorded. PM, PMG, and PMGH kept

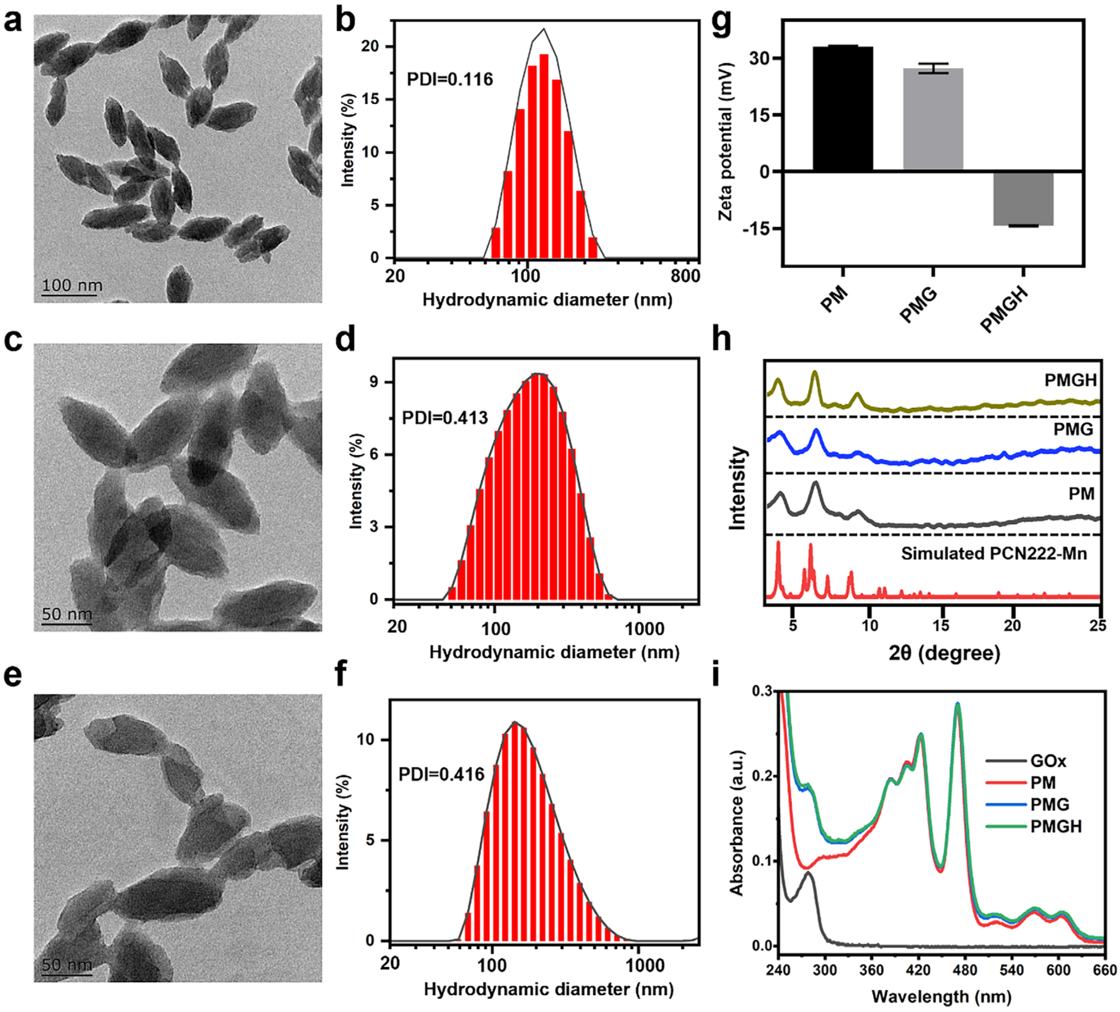

Figure 2. Synthesis and characterization of enzyme-nanozyme hybrid. a) TEM image of PM. Scale bar: 100 nm. b) Size distribution of PM. c) TEM image of PMG (weight ratio of PM: GOx sets as 1:0.1). Scale bar: 50 nm. d) Size distribution of PM (weight ratio of PM: GOx sets as 1:0.1). e) TEM image of PMGH (weight ratio of PMG: HA sets as 5:1). Scale bar: 50 nm. f) Size distribution of PMGH (weight ratio of PMG: HA sets as 5:1). g) Zeta potential of PM, PMG, and PMGH. Each error bar represents the standard deviation of four independent measurements. h) XRD patterns of PM, PMG, PMGH, and simulated PCN22-Mn. i) UV–vis spectra of GOx, PM, PMG, and PMGH.

the characteristic peak at ≈480 nm, which was referred to the presence of TCPP-Mn; the peak near 280 nm was presented as the GOx in PMG and PMGH, which could corroborate the modification of GOx (Figure 2i). All these results confirmed the successful synthesis of PMGH.

2.2. Properties of ENCAT System

Next, the properties of ENCAT system were explored for further biomedical application. First, the stability of PM was investigated by incubating PM with different solutions such as cell culture medium, phosphate buffer (10 mm PBS, pH 7.4), and GSH (5 mm). TEM imaging exhibited that PM could be disassembled in culture medium, GSH, and PBS with long-time incubation (**Figure 3**a; Figure S4, Supporting Information). This disassembling ability exhibited good biosafety for biomedical application. Subsequently, the catalytic activities were explored. As shown in Figure 3b, natural enzyme GOx could catalyze the oxidation of glucose producing H_2O_2. The produced H_2O_2 could be converted into O_2 by nanozyme PM, forming a cascade catalysis. The CAT-like activity of nanozyme PM was evaluated by monitoring the dissolved oxygen generation in the presence of H_2O_2. As shown in Figure 3c, the content of dissolved oxygen in both PM and PMG increased, which testified the CAT-like activity of PM. While dissolved oxygen in PMGH group did not obviously increased, in HAase-treated PMGH group (HAase could degrade the HA to release PMG, termed as HAase-treated PMGH), the CAT-like activity was recovered. The activity recovery could be attributed to the degradation of HA by HAase and also demonstrated HA protection for PMGH. Meanwhile, their CAT-like activity was also detected by using a dopamine-enabled universal assay.[42] PMGH demonstrated the lowest CAT-like activity (Figure S5, Supporting Information), which was consistent with the dissolved oxygen detection.

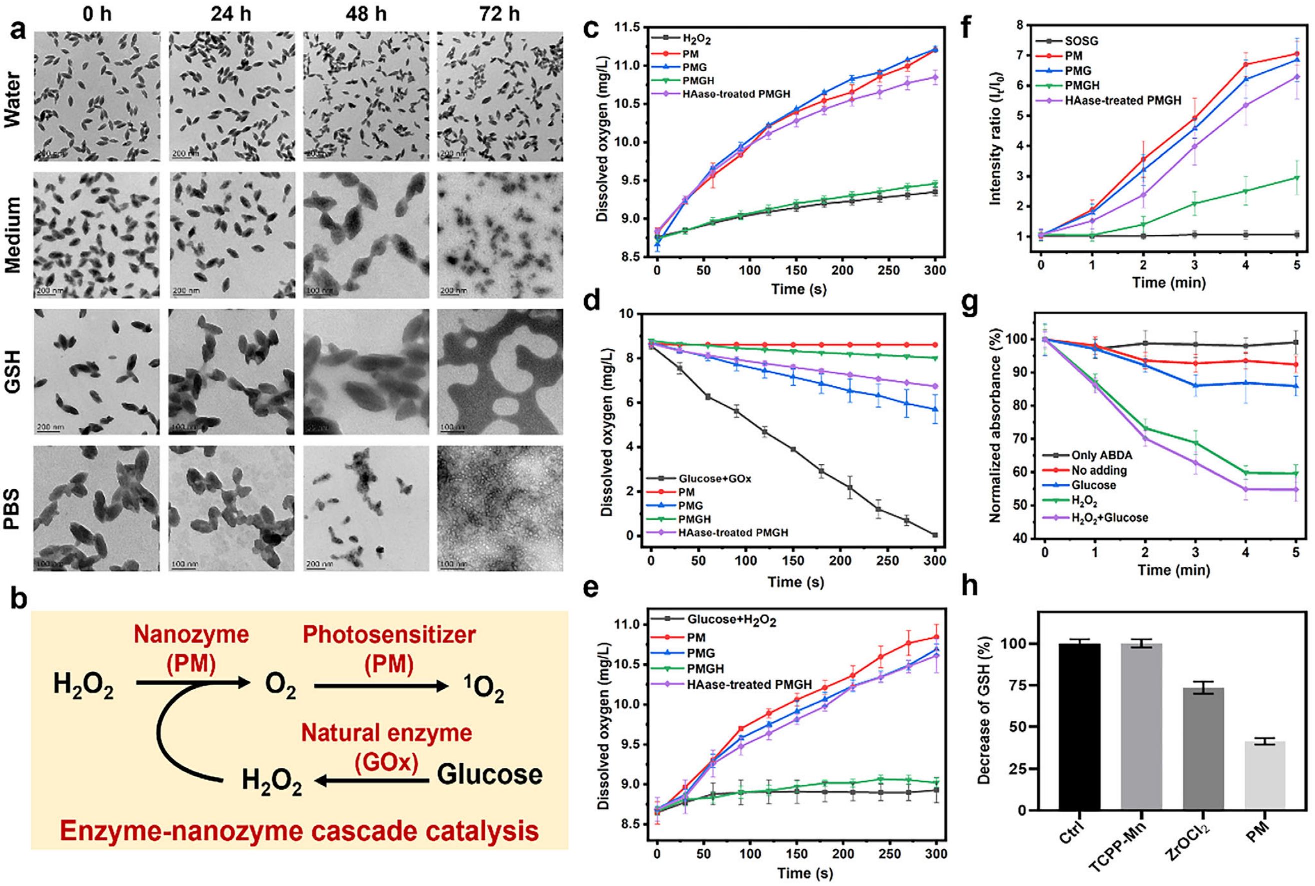

Figure 3. Properties of enzyme-nanozyme cascade catalytic system. a) TEM images of PM with indicated treatments (pH 7.4 10 mM PBS, 5 mM GSH, and fully cell culture medium) and time points (0, 24, 48, and 72 h). b) Schematic description of enzyme-nanozyme cascade catalysis. c) Analysis of catalase activity by measuring dissolved oxygen, using H_2O_2 as the primary substrate. d) Analysis of cascade catalysis by measuring dissolved oxygen, using glucose as primary substrate. e) Analysis of cascade catalysis by measuring dissolved oxygen, using both glucose and H_2O_2 as substrates. f) PDT efficacy of PM, PMG, PMGH, and HAase-treated PMGH by measuring $^1O_2$ generation using SOSG as a probe, with 660 nm laser exposure (0.2 W cm^{-2}) for different time points. g) PDT efficacy of HAase-treated PMGH under hypoxia by using ABDA as sensor, with 660 nm laser exposure (0.2 W cm^{-2}) for different time points. h) GSH decreasing analysis by indicated treatments. Each error bar represents the standard deviation of four independent measurements.

Subsequently, the activity of GOx was investigated by co-incubating with glucose (Figure 3d,e). In the Glucose + GOx alone group, the oxygen content decreased sharply, while in the PMG and HAase-treated PMGH groups (with glucose), the oxygen content declined slowly, and at a later stage total oxygen content was twice more than Glucose + GOx group. This trend was attributed to enzyme-nanozyme mediated a cascade catalysis: natural GOx mediated oxygen consumption and H_2O_2 generation, and PM nanozyme catalyzed the produced H_2O_2 to partially recover oxygen. Additionally, gluconic acid was generated in natural enzyme mediated catalysis. The decreased pH value of reaction solution in HAase-treated PMGH group also verified the occurrence of catalytic reaction (Figure S6, Supporting Information). From oxygen recovery and pH decrease mentioned above, a cascade catalysis was demonstrated.

Because enzyme-nanozyme mediated cascade catalysis could generate oxygen, the key substrate for PM-mediated PDT, therefore production of single oxygen ($^1O_2$) was evaluated. Initially, SOSG (Singlet Oxygen Sensor Green) as a $^1O_2$ probe was used for studying photodynamic property in normal oxygen condition. PM, PMG, and HAase-treated PMGH kept a similar trend with the laser irradiation and demonstrated the photodynamic function, while PMGH showed less $^1O_2$ production due to the HA protection (Figure 3f). The $^1O_2$ generation was further confirmed via electron paramagnetic resonance (EPR) measurment by using 2,2,6,6-tetramethyl-4-piperidone (TEMP) as a capturing probe (Figure S7, Supporting Information). To explore whether the cascade catalysis would facilitate PDT in hypoxic environment by using AneroPack and an anaerobic bag, water-soluble ABDA (9,10-Anthracenediyl-bis(methylene) dimalonic acid) was chosen for $^1O_2$ detection. As shown in Figure 3g, there was less $^1O_2$ production when ABDA alone was mixed with HAase-treated PMGH. While adding glucose in the mixture (ABDA with HAase-treated PMGH), the production of $^1O_2$ increased. Adding H_2O_2 to the mixture (ABDA with HAase-treated PMGH), there was an obvious $^1O_2$ production. Supplementing both glucose and H_2O_2 to the mixture (ABDA with HAase-treated PMGH), the largest $^1O_2$ production was achieved. From above results, we ascertained that our design could enhance PDT by a cascade catalysis. $^1O_2$ as ROS could induce cell death, but cellular antioxidants would decrease ROS-induced cytotoxicity. Coincidentally, some reports demonstrated that Zr had the ability for GSH consumption,[43] so we studied the interactions between PM and GSH. After incubation, PM could decrease the GSH content, which could be reasoned for the GSH-mediated PM disassembly (Figure 3h). Combining $^1O_2$ production and GSH consumption together, our design holds promise for the following therapeutical applications.

2.3. Cellular Performances of ENCAT System

Regarding performances of PMGH in vitro, herein we explored its cellular performance. Capacity of cell uptake was first evaluated by incubating 4T1 cells (mouse breast tumor cells) and L02 cells (as a representative normal cell for cell uptake analysis) with our materials. Rhodamine B-labelled materials were incubated with 4T1 cells and L02 cells for 6 h, respectively. Then confocal imaging was performed. For 4T1 cells, the PMGH-treated group demonstrates the highest uptake due to HA-mediated targeting (**Figure 4a**; Figure S9, Supporting Information), while for normal L02 cells, they exhibited low cell uptake in each treatment (Figures S8 and S9, Supporting Information). After HA-mediated high tumor cell uptake analysis, cell viability was detected with different treatments. PM did not show any obvious cytotoxicity even at higher concentrations (Figure S10, Supporting Information), while PMG (weight ratio of PM: GOx = 1:0.1) demonstrated cytotoxicity (Figure S11, Supporting Information). Even higher cytotoxicity was observed with more GOx assembly (weight ratios of PM:GOx as 1:0.2 and 1:0.5) (Figure S10, Supporting Information), so PM:GOx = 1:0.1 was chosen for both cellular and animal experiments. Given the GOx-introduced cytotoxicity, PMGH also showed dose-dependent cytotoxicity (Figure 4b). Due to the photodynamic effect of porphyrin structure, this cytotoxicity was boosted with laser irradiation (0.2 W cm^{-2}, 5 min irradiation by 660 nm laser) (Figure 4c).

To further verify the photodynamic effect, cellular ROS was measured by flow cytometry using DCFH-DA (2′,7′-dichlorodihydrofluorescein diacetate) as a ROS probe. 4T1 cells were incubated with different materials (20 µg mL^{-1}) for 6 h, and cells were irradiated with a 660 nm laser (0.2 W cm^{-2}, 5 min); after irradiation, cells were incubated with DCFH-DA for 20 min and then harvested for flow cytometry analysis. All treated groups show higher ROS levels when compared with the control group (Figure 4d), attributing to the porphyrin structure-mediated photodynamic effect. This result was further supported by staining analysis of dead cells (Figure S12, Supporting Information).

Based on the photodynamic effect of our materials in normal oxygen condition, we further explored whether the enzyme-nanozyme mediated-cascade catalysis would enhance PDT in hypoxic environment by using AneroPack and anaerobic bag. The cellular ROS level was monitored in hypoxic condition by using a confocal microscope (Figure 4e,f): PM showed low ROS production due to hypoxia; PMG demonstrated higher ROS level based on self-oxygen generation by the enzyme-nanozyme mediated cascade catalysis; PMGH exhibited the highest ROS generation due to HA-mediated targeting and cascade catalyzed-O_2 generation. From cellular performance, our designed enzyme-nanozyme would be beneficial for cascade catalysis-enhanced PDT.

2.4. Anti-Tumor Activity of ENCAT System at Cellular Level

In view of excellent ROS generating activity within cells, we further explored the anti-tumor activity of ENCAT system (**Figure 5a**). Glucose is usually metabolized into lactate through glycolysis. In our design, cellular glucose also acted as the primary substrate for our ENCAT system. Glucose uptake and lactate acid excretion as main indicators of tumor glucose metabolism, therefore, we monitored contents of both glucose and lactate acid in culture supernatant. As shown in Figure 5b, glucose content from culture supernatant in PMG and PMGH groups were lower than PM group. Lactate content from culture supernatant in both PMG and PMGH were also lower than PM group (Figure 5c). Based on the decrease of glucose and lactate in culture supernatant, we regarded that our PMGH could compete glucose consumption with cellular glucose metabolism, which could induce starvation therapy.

From above cascade catalysis-enhanced PDT effect (Figure 4e,f) and catalytic consumption of glucose (**Figure 5b,c**), we regarded that these two would promote synergistic therapy. Exceptionally, PDT-mediated cell death would cause immunogenic cell death (ICD), which could activate/promote the immunotherapy.[44,45] Therefore, we evaluated these ICD-associated molecules including adenosine triphosphate (ATP), calreticulin (CRT), and high-mobility group box 1 (HMGB1). PM, PMG, and PMGH-treated groups with laser irradiation demonstrated the high levels of ATP (Figure S13a, Supporting Information) and HMGB1 release (Figure 5d; Figure S14a, Supporting Information), as well as high levels of CRT exposure (Figure 5e; Figure S14b, Supporting Information); but for PM, PMG, and PMGH-treated groups without laser irradiation, levels of these molecules were lower (Figures S13b,S15, and S16, Supporting Information). Furthermore, PMGH-treated group with laser irradiation demonstrated the highest levels of ATP and HMGB1 release, and the highest level of CRT exposure, we regarded these were due to more PMGH cellular accumulation-enhanced ICD (Figure 5d,e; Figure S14, Supporting Information).

Having demonstrated the ENCAT system-induced changes in ICD molecules, next we explored its immune activation with a Transwell co-culture system. 4T1 cells were cultured in upper channel and Raw 264.7 cells as macrophages were cultured in down channel (Figure 5g,h). Representative cytokines including interferon γ (IFN γ) and tumor necrosis factor α (TNF α), as indicators of immune activation/promotion, were monitored (Figure 5f). In PM, PMG, and PMGH-treated groups without laser irradiation, increase of IFN γ and TNF α was not significant (Figures S17 and S18, Supporting Information). Furthermore, these cytokines in PMGH and PMG groups (with laser irradiation) were higher than PM group (with laser irradiation). We regarded these were due to the synergistic performance of PM-mediated PDT and GOx-mediated starvation. In addition, Mn^{2+} could enhance STING (stimulator of interferon genes) immune signal pathway,[46] IFN β as an indicator of STING signal pathway

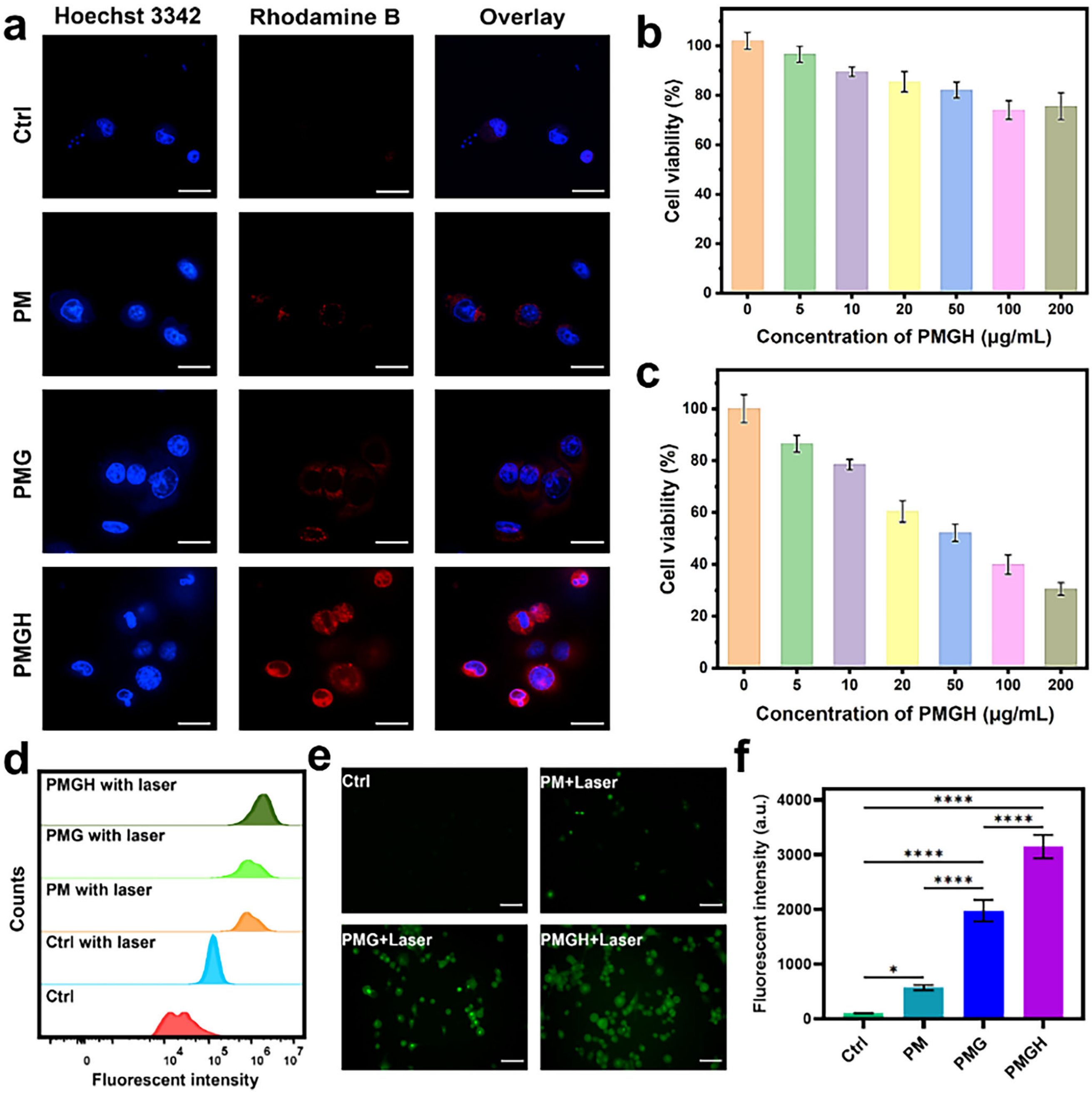

Figure 4. Cellular properties of ENCAT system. a) Cell uptake ability analysis for 4T1 cells by confocal imaging. Hoechst 3342 represents cells' nuclei and red fluorescence represents the Rhodamine B-labelled materials. Scale bar: 50 μm. b) Cell viability of PMGH at different concentrations. Each error bar represents the standard deviation of four independent measurements. c) Cell viability of PMGH at different concentrations with laser (0.2 W cm^{-2}, 5 min). Each error bar represents the standard deviation of four independent measurements. d) Flow cytometry and e) confocal imaging of ROS generation by indicated treatments. DCFH-DA as an ROS fluorescent probe. Scale bar: 100 μm. f) Quantification of ROS generation by indicated treatments. Each error bar represents the standard deviation of four independent measurements. Ordinary one-way ANOVA was used for discrepancy analysis ($^*p < 0.05$, $^{**}p < 0.01$, $^{***}p < 0.001$, $^{****}p < 0.0001$).

was detected. The tendency of IFN β was similar to IFN γ and TNF α in PM, PMG, and PMGH-treated groups with/without laser irradiation (Figure S19, Supporting Information).

From cellular performances mentioned above, our ENCAT system clearly demonstrated an enhance-PDT by enzyme-nanozyme mediated cascade catalysis, and a synergistic therapy by combining enhanced-PDT, starvation therapy, and activated/promoted-immunotherapy together. Collectively, these would be beneficial to further anti-tumor activity in vivo.

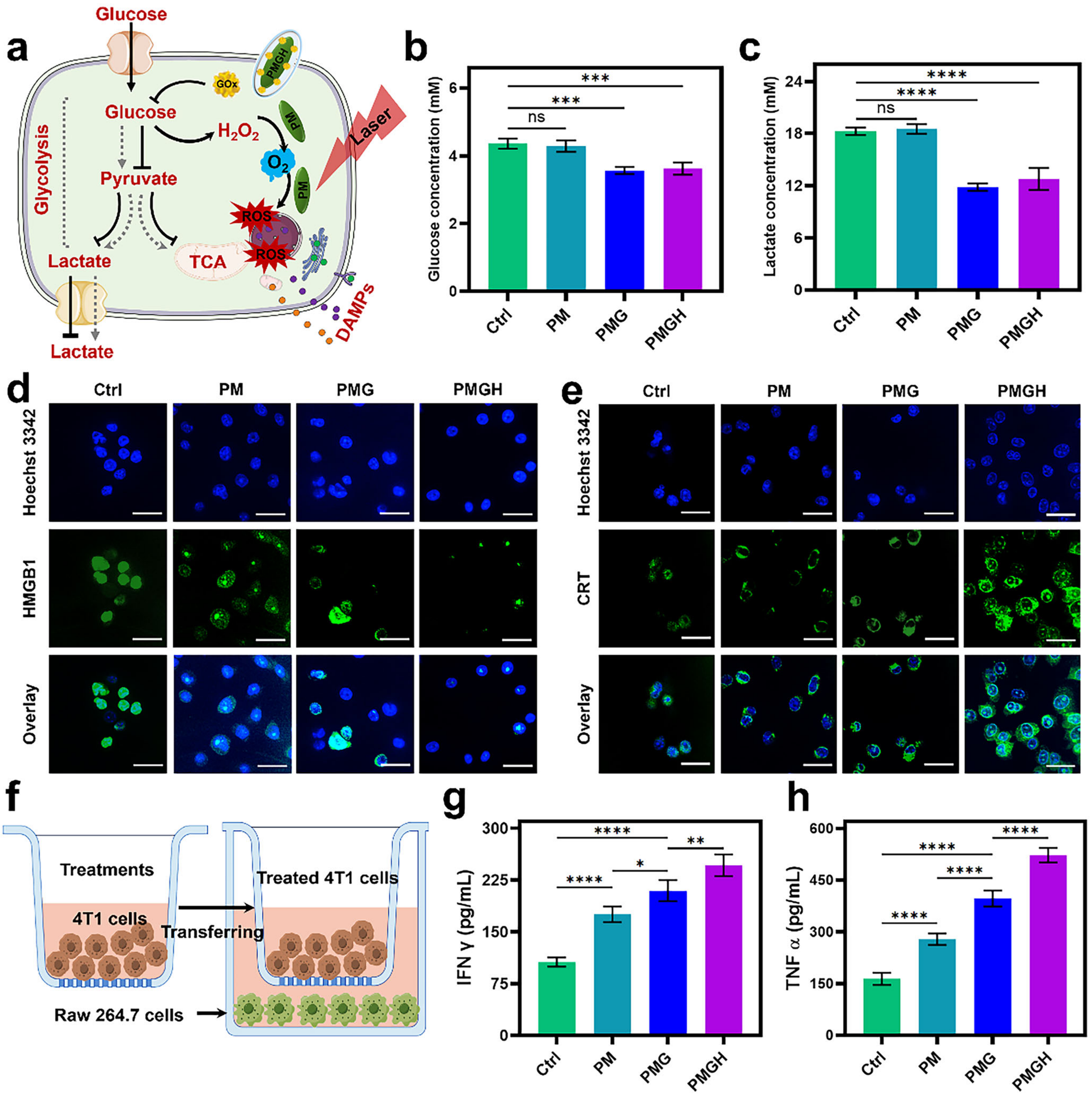

Figure 5. Functional analysis of ENCAT system. a) Schematic description of cellular performance by PMGH treatment. Glucose content (b) and lactate content (c) in culture supernatants by indicated treatments. Analysis of HMGB1 release (d) and CRT exposure (e) in indicated treatments with laser irradiation (0.2 W cm^{-2}, 5 min). Scale bar: 50 µm. f) Schematic description of immune activation by Transwell co-culture system. Detection of IFN γ (g) and TNF α (h) in each treated culture supernatant. Each error bar represents the standard deviation of four independent measurements. Ordinary one-way ANOVA was used for discrepancy analysis ($*p < 0.05$, $**p < 0.01$, $***p < 0.001$, $****p < 0.0001$, ns: not significant).

2.5. ENCAT System Mediated Anti-Tumor Ability

In view of ENCAT system's performances at cellular levels, 4T1 breast tumor cells bearing mouse model was constructed to evaluate its anti-tumor ability in vivo. The biocompatibility of ENCAT system was first evaluated. Hemolysis was investigated by incubating PMGH with mouse blood. PMGH showed low percentage of hemolysis even at high concentration (100 µg mL^{-1}) (Figure S20, Supporting Information). Tumor bearing mice's weight changes (Figure S21, Supporting Information) and major organs' histopathological staining (Figure S22, Supporting Information) were also monitored after different treatments, indicating that all treatments showed no obvious side effect and demonstrated good biocompatibility. Additionally, HA targeting ability was tested by fluorescent imaging (Figure S23, Supporting Information). PMGH demonstrated great tumor accumulation and kidney excretion.

Based on good biocompatibility and tumor targeting ability, anti-tumor ability was investigated (**Figure 6**a). Tumor volume changing and weight of dissected tumor after different treatments varied across groups (Figure 6b–d): PMGH + Laser group demonstrated the strongest anti-tumor ability, followed by PMG + Laser and PMGH groups, while other groups showed lower anti-tumor ability. Based on anti-tumor ability (Figure 6b–d) and cellular immune activation/promotion (Figure 5d–h), herein we explored immunotherapy of ENCAT system in vivo. Representative cytokines including IFN γ, IFN β, and TNF α from peripheral blood of treated mice were measured. As shown in Figure S24 (Supporting Information), these cytokines exhibited similar tendency between groups and showed positive correlation with anti-tumor ability. Generally, these cytokines are associated with immune activation/promotion. T cells' infiltration in tumor areas was stained by immunofluorescent analysis (Figure 6e): PMGH+Laser group demonstrated the largest T cells' infiltration including both CD4 and CD8 T cells, which was also positively associated with anti-tumor ability. Given that ENCAT system could activate/promote immunotherapy, we further constructed tumor lung metastatic model to investigate its anti-metastatic ability (Figure 6f). PMGH + Laser group demonstrated the least metastatic nodules due to the best immune-activation/promotion (Figure 6g; Figure S25, Supporting Information).

3. Conclusion

To address the limitations of current single catalytic therapies, we developed an enzyme-nanozyme cascade catalysis (ENCAT)-enhanced tumor therapy by ingeniously combining a natural enzyme (GOx) and a nanozyme (PCN222-Mn). Moreover, we endowed the ENCAT system with active targeting capacity through HA modification. Because of HA targeting capacity, our PMGH accumulated effectively in tumor area. Upon entering tumor cells, GOx mediated glucose consumption, producing H_2O_2. PCN222-Mn catalyzed the produced H_2O_2 into oxygen. Collectively, these achieved a cascade catalysis for O_2 generation. The generated O_2 enhanced PCN222-Mn-mediated PDT, which then activated immunotherapy. Meanwhile, GOx-mediated glucose consumption induced starvation therapy. By integrating PDT, immunotherapy, and starvation together, an enhanced synergistic therapy was achieved. Both in cellular and animal models, our ENCAT system demonstrated a strong anti-tumor ability. To sum up, our ENCAT system not only surmounted limitations of single catalytic therapies but also achieved a cascade catalysis-enhanced tumor therapy through the integration of natural enzyme and nanozyme, providing a new strategy for tumor treatment.

4. Experimental Section

Synthesis of TPP-COOMe and TCPP-Mn: TPP-COOMe [5,10,15,20-tetrakis (4-methoxycarbonylphenyl) porphyrin] was synthesized according to reported methods.[36–39] Briefly, methyl *p*-formylbenzoate (14 g) was dissolved in propionic acid (200 mL), then pyrrole (6 mL) was dropwisely added and refluxed for 12 h in the dark. After complete reaction, the product was obtained and washed with methanol and THF several times. TCPP-Mn was synthesized as follows: TPP-COOMe (0.657 g) and $MnCl_2 \cdot 4H_2O$ (1.92 g) were dissolved in DMF (100 mL) and were refluxed for 6 h at 160 °C. The mixture was cooled to room temperature. 150 mL of H_2O was added and further stirred for 1 h. The precipitate was collected and washed with H_2O three times. The obtained dark solid was dissolved in methanol (60 mL), THF (60 mL), and KOH solution (6.82 g KOH in 60 mL of H_2O), and then the mixed solution was refluxed at 85 °C for 12 h in the dark. THF and methanol were removed by rotary evaporator and then 1 м HCl was added to the solution to fully acidify the precipitate. The obtained dark solution was further filtered, and washed with water, and then dried in a vacuum.

Synthesis of PCN222-Mn, PCN222-Mn@GOx, and PCN222-Mn@GOx/HA: The PCN222-Mn (i.e., PM) nanoparticle was synthesized according to a previous method[37] TCPP-Mn (20 mg), $ZrOCl_2 \cdot 8H_2O$ (60 mg), and benzoic acid (520 mg) were dissolved in DMF (20 mL), and the mixture was stirred at 90 °C for 5 h. After cooling to room temperature, PM was obtained by centrifugation (13 000 rpm, 40 min) followed by washing with DMF several times, and stored for later use. The PCN222-Mn@GOx (i.e., PMG) was synthesized with 4 mL of PCN222-Mn (1 mg mL^{-1}) and 4 mL of GOx (with different concentrations of 0.1, 0.2, and 0.5mg mL^{-1}) by stirring vigorously for 20 min. Then, PCN222-Mn@GOx/HA was synthesized based on PMG. The PCN222-Mn@GOx/HA (i.e., PMGH) was synthesized by adding HA into PMG. 2 mL of HA (10 mg mL^{-1}) was added in 8 mL of 0.5 mg mL^{-1} PMG solution, the mixture was kept stirring 30 min for complete modification. The obtained solution was washed with water three times (13 000 rpm, 40 min) and stored for further use. Rhodamine B-labelled materials were prepared by mixing Rhodamine B with PM together at ratio of 1:10, then was modified with GOx or HA for cell uptake analysis.

Degradation Assay of PM: Degradation of PM was performed by incubating PM with different solutions, including water, PBS (10 mм, pH 7.4), GSH (5 mм), and complete cell culture medium (containing 10% fetal bovine serum). Typically, 2 mL of PM (20 µg mL^{-1}) was mixed with above solutions, respectively. Then hydrodynamic diameter and morphology of mixture were monitored using DLS analysis and TEM imaging.

Measurement of CAT-Like Activity and Cascade Catalysis: The catalase (CAT)-like activity of nanoparticles was evaluated. Typically, 20 µg mL^{-1} nanoparticles were incubated with 5 mM H_2O_2, and the dissolved oxygen content was monitored in 5 min and recorded at time points using SevenExcellence Multiparameter.

Cascade catalysis was also assessed by monitoring oxygen generation. 20 µg mL^{-1} nanoparticles were incubated with 0.1 mg mL^{-1} glucose without H_2O_2, and the oxygen content was recorded at time points; meanwhile, 20 µg mL^{-1} nanoparticles were incubated with 0.1 mg mL^{-1} glucose and 5 mм H_2O_2, and the oxygen content was recorded at time points. For a dopamine-enabled universal assay for CAT-like activity analysis,[42] 5 µL of sample with different concentrations, 90 µL of Tris buffer (10 mм, pH 8.5), 100 µL of dopamine (2 mg mL^{-1}), and 5 µL of H_2O_2 were mixed into 96-well plate. Then the plate was quickly transferred into an anaerobic bag (with AnaeroPack for hypoxic microenvironment) and incubated 30 min for absorbance at 405 nm.

Measurement of Singlet Oxygen ($^1O_2$) Generation: 20 µg mL^{-1} several nanoparticles, including PM, PMG, PMGH, and HAase-treated PMGH (PMGH was treated with HAase for HA degradation), were mixed with SOSG (5 mм). The solutions were then irradiated with a 660 nm laser (0.2 W cm^{-2}). $^1O_2$ generation was recorded at time points with fluorescent intensity (Ex/Em = 488/525 nm). The $^1O_2$ generation was also detected by electron paramagnetic resonance (EPR) using 2,2,6,6-tetramethyl-4-piperidone (TEMP) as a capturing probe, with a 660 nm laser (0.2 W cm^{-2}) for 5 min. Cascade catalysis-mediated $^1O_2$ generation was carried out in an anaerobic bag. HAase-treated PMGH was incubated with water-soluble ABDA probe for $^1O_2$ detection by incubating HAase-treated PMGH with or without glucose/H_2O_2. In a typical test, mixture of 20 µg mL^{-1} HAase-treated PMGH and 0.2 mм ABDA was evacuated for 30 min, then glucose/H_2O_2 was added to the solution and irradiated by 660 nm laser (0.2 W cm^{-2}). $^1O_2$ generation was recorded at time points with UV–vis absorbance at 400 nm.

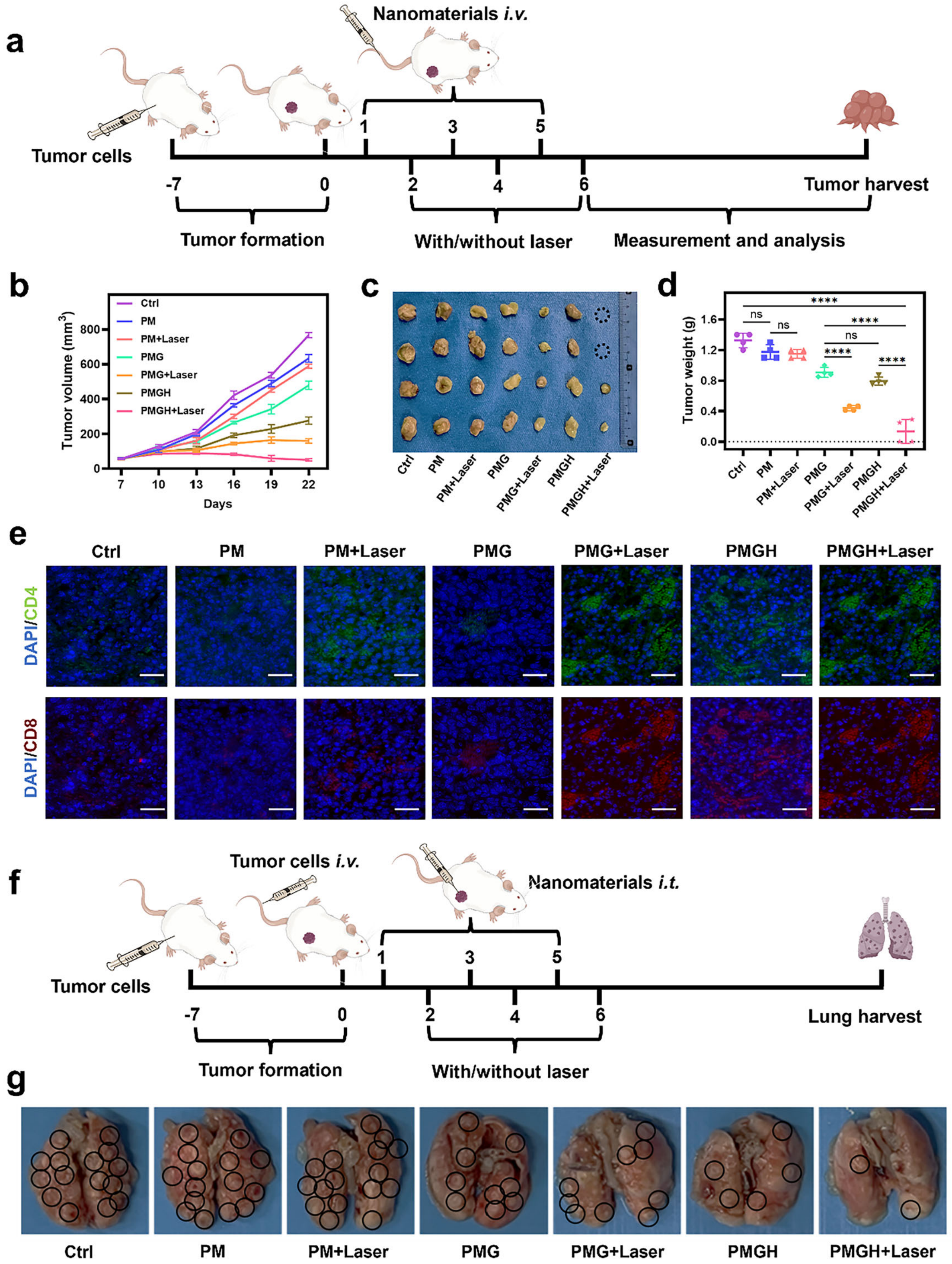

Figure 6. Anti-tumor and anti-metastatic ability. a) Schematic description of subcutaneous tumor model construction and treatments. b) Change of tumor volume in time points by indicated treatments. Each error bar represents the standard deviation of four independent measurements. c) Photo of dissected tumor by indicated treatments. d) Weight of dissected tumors by indicated treatments. Each error bar represents the standard deviation of four independent measurements. Ordinary one-way ANOVA was used for discrepancy analysis (*$p < 0.05$, **$p < 0.01$, ***$p < 0.001$, ****$p < 0.0001$, ns: not significant). e) CD4 and CD8 T cells' infiltration by immunofluorescent analysis, green fluorescence represents CD4 marker, red fluorescence represents CD8 marker. Scale bar: 100 µm. f) Schematic description of tumor metastatic model construction and treatments. g) Dissected lungs for metastatic analysis, black circle represents metastatic nodule. For subcutaneous tumor model, 4T1 cells subcutaneous injection for each mouse, 5 mg kg^{-1} nanomaterials intravenous injection for treatments, 660 nm laser for irradiation at 0.2 W cm^{-2}, 5 min. For tumor metastatic model, 4T1 cells subcutaneous injection and 4T1 cells intravenous injection for each mouse, 5 mg kg^{-1} nanomaterials intratumor injection for treatments, 660 nm laser for irradiation at 0.2 W cm^{-2}, 5 min.

Cell Culture, Cell Viability, and Cell Uptake: For cell culture, 4T1 cells, and L02 cells were cultured with high-glucose Dulbecco's modified Eagle's medium (DMEM) culture medium containing 5% fetal bovine serum and 1% penicillin-streptomycin at 37 °C in a 5% CO_2. For cell viability, cells were subcultured into 96-well plates with a seeding density of 8 × 10^3 cells well^{-1}. When cells' confluence was up to 70%, materials were added for another 24 h co-incubation with different concentrations (5, 10, 20, 50, 100, and 200 µg mL^{-1}). Cell viability was evaluated by CCK-8. For cell uptake ability, refreshed 4T1 cells were seeded into confocal plates. When cell density was up to 60%, Rhodamine B-labelled materials were incubated with cells for 6 h, then cells were imaged using CLSM.

Cellular ROS Detection and Dead Cell Staining: $^1O_2$ sensor like SOSG is usually hard to enter into cells and cell culture medium has some influence on $^1O_2$ sensor, hence DCFH-DA as a broad probe for ROS detection was chosen here for cellular ROS ($^1O_2$) detection. Cells were co-incubated with 20 µg mL^{-1} materials for 6 h, and then irradiated with 660 nm laser (0.2 W cm^{-2}, 5 min). Cellular ROS was evaluated both using CLMS and flow cytometry, with DCFH-DA as the probe. For dead cell staining, cells were co-incubated with 20 µg mL^{-1} materials for 6 h, irradiated with 660 nm laser (0.2 W cm^{-2}, 5 min), and then stained with propidium iodide (PI) for CLSM imaging.

Detection of Glucose and Lactate in Culture Supernatant: Glucose and lactate detection were performed. The culture supernatant after materials' treatments was collected for the glucose consumption and lactate excretion analysis. For glucose consumption detection, 100 µL of culture supernatant was transferred to 96-well plates, and then a working solution of glucose detection was added to each well. Later, the reaction solution was fully mixed and incubated at 37 °C for 30 min. Finally, absorbance at 450 nm was measured by a microplate reader. Lactate detection was performed following the same procedures, using a lactate detection kit.

Cellular Immune Activation by Transwell System: Cellular immune activation was detected by Transwell system. 4T1 and Raw 264.7 cells were cultured in upper and down channels, respectively. The 4T1cells were treated with materials and lasers (660 nm, 0.2 W cm^{-2}, 5 min), then cultured with Raw 264.7 cells by Transwell system. Cytokines in culture supernatant were detected by enzyme-linked immunosorbent assay (ELISA) kits, including TNF α, IFN γ, and IFN β. The detecting process was operated by standard protocol provided with each kit.

Anti-Tumor and Anti-Metastatic Ability: The animal experiments were approved by the Institutional Animal Care and Use Committee (IACUC) of Nanjing University (2 112 015). Female BLAB/c mice were supplied by Beijing Vital River Laboratory Animal Technology Co., Ltd. (China). After 7 days' acclimatization, the mice were subjected to tumor model. For primary tumor model, 4T1 cells were harvested and injected into the right flank of mice with a density of 3 × 10^6 cells/mouse. When the tumor volume (the volume of tumor = length × width × width/2, length and width were measured by using a digital caliper) reached 50 mm^3, mice were separated into groups and treated with materials by intravenous injection (dosage of all materials at 5 mg kg^{-1}). After 12 h of materials' injection, mice were given laser irradiation in laser groups (660 nm for 5 min at 0.2 W cm^{-2}). Mice weight and tumor volume were recorded for anti-tumor analysis. After treatments, each tumor was dissected for immunofluorescent analysis. Major organs were harvested for biosafety estimation, including heart, liver, spleen, lung, and kidney.

For metastatic model, female BLAB/c mice were also chosen for model construction. Mice were fed in a standard SPF environment. The 4T1 subcutaneous tumor model was obtained using the same procedure as mentioned above. After the tumor formation, 4T1 cell suspension was intravenously injected into mice (1 × 10^6 cells/mouse). Materials were injected into tumor directly, and laser was irradiated (660 nm for 5 min at 0.2 W cm^{-2}) in laser-needed groups. Lastly, the lungs were dissected for anti-metastasis analysis. The metastatic nodules were counted. The lungs were stained by using the hematoxylin and eosin (H&E) staining.

Immune Activation Analysis In Vivo: To explore the anti-tumor and anti-metastatic mechanisms, CD4 and CD8 T cells' infiltration in dissected tumor was explored by immunofluorescent analysis. The dissected tumors were mounted by OCT compound for 5 µm slices. The slices were used for immunofluorescent analysis following standard protocols, and were imaged by a confocal microscope. The fluorescent intensity was analyzed by Image J and data were obtained by Origin. Cytokines were also measured for evaluating the immune activation. Briefly, the peripheral blood of mouse was collected and left for clotting, and upper serum was used for cytokines' detection, including TNF α, IFN γ, and IFN β. The detecting process were operated by standard protocol which was provided by each kit. Each experiment was performed four times independently.

Statistical Analysis: The GraphPad Prism software (version 9.0) was applied to perform statistical analysis. Data were presented as mean values ± SEM Each error was represented at least four independent experiments. Ordinary one-way ANOVA was used for discrepancy analysis ($^*p < 0.05$, $^{**}p < 0.01$, $^{***}p < 0.001$, $^{****}p < 0.0001$, ns: not significant). Ordinary one-way or two-way analysis of variance (ANOVA) followed by Tukey's post-hoc tests were used to assess the statistical significance ($^*p < 0.05$, $^{**}p < 0.01$, $^{***}p < 0.001$, $^{****}p < 0.0001$, ns: not significant).

Supporting Information

Supporting Information is available from the Wiley Online Library or from the author.

Acknowledgements

M.Z. and J.F. contributed equally to this work. This work was funded by the National Natural Science Foundation of China (22374071), the Jiangsu Provincial Key R&D Program (BE2022836), the National Key R&D Program of China (2019YFA0709200 and 2021YFF1200700), the Open Funds of NMPA Key Laboratory for Biomedical Optics (20240001), the PAPD Program, the State Key Laboratory of Analytical Chemistry for Life Science (5431ZZXM2306), and the Fundamental Research Funds for the Central Universities (202200325 and 021314380228). Thanks Figdraw (www.figdraw.com) for help in drawing schemes. Writing was polished with the assistance of OpenAI.

Conflict of Interest

The authors declare no conflict of interest.

Data Availability Statement

The data that support the findings of this study are available from the corresponding author upon reasonable request.

Keywords

cascade catalysis, catalytic therapy, enzyme-nanozyme, metal–organic framework (MOF), synergetic therapy

Received: October 11, 2024
Revised: January 12, 2025
Published online: January 19, 2025

---

[1] T. Finkel, M. Serrano, M. A. Blasco, *Nature* **2007**, *448*, 767.
[2] R. Blum, Y. Kloog, *Cell Death Dis.* **2014**, *5*, e1065.
[3] S. Maman, I. P. Witz, *Nat. Rev. Cancer* **2018**, *18*, 359.
[4] Q. Chen, C. Liang, X. Sun, J. Chen, Z. Yang, H. Zhao, L. Feng, Z. Liu, *Proc. Natl. Acad. Sci. U. S. A.* **2017**, *114*, 5343.
[5] X. Liu, Y. Li, K. Wang, Y. Chen, M. Shi, X. Zhang, W. Pan, N. Li, B. Tang, *Nano Lett.* **2021**, *21*, 7862.

[6] Y. Wan, L.-H. Fu, C. Li, J. Lin, P. Huang, *Adv. Mater.* **2021**, *33*, 2103978.
[7] Y. Luo, Y. Li, Z. Huang, X. Li, Y. Wang, J. Hou, S. Zhou, *Nano Lett.* **2022**, *22*, 6418.
[8] J. An, S. Tang, G. Hong, W. Chen, M. Chen, J. Song, Z. Li, X. Peng, F. Song, W.-H. Zheng, *Nat. Commun.* **2022**, *13*, 2225.
[9] C. Zhang, X. Hu, L. Jin, L. Lin, H. Lin, Z. Yang, W. Huang, *Adv. Healthcare Mater.* **2023**, *12*, 2300530.
[10] P. Zhu, Y. Pu, M. Wang, W. Wu, H. Qin, J. Shi, *J. Am. Chem. Soc.* **2023**, *145*, 5803.
[11] C. Shi, M. Li, Z. Zhang, Q. Yao, K. Shao, F. Xu, N. Xu, H. Li, J. Fan, W. Sun, J. Du, S. Long, J. Wang, X. Peng, *Biomaterials* **2020**, *233*, 119755.
[12] L.-H. Fu, C. Qi, J. Lin, P. Huang, *Chem. Soc. Rev.* **2018**, *47*, 6454.
[13] F. Duan, W. Jin, T. Zhang, Y. Sun, X. Deng, W. Gao, *Adv. Mater.* **2023**, *35*, 2209765.
[14] A. Najafi, M. Keykhaee, H. Khorramdelazad, M. Y. Karimi, L. Nejatbakhsh Samimi, N. Aghamohamadi, M. Karimi, R. Falak, M. Khoobi, *Biomed. Pharmacother.* **2022**, *153*, 113483.
[15] L. Ma, F. Jiang, X. Fan, L. Wang, C. He, M. Zhou, S. Li, H. Luo, C. Cheng, L. Qiu, *Adv. Mater.* **2020**, *32*, 2003065.
[16] Y. Huang, J. Ren, X. Qu, *Chem. Rev.* **2019**, *119*, 4357.
[17] Y. Zhang, G. Wei, W. Liu, T. Li, Y. Wang, M. Zhou, Y. Liu, X. Wang, H. Wei, *Nat. Rev. Methods Primers* **2024**, *4*, 36.
[18] R. Zhang, B. Jiang, K. Fan, L. Gao, X. Yan, *Nat. Rev. Bioeng.* **2024**, *2*, 849.
[19] B. Xu, Y. Cui, W. Wang, S. Li, C. Lyu, S. Wang, W. Bao, H. Wang, M. Qin, Z. Liu, W. Wei, H. Liu, *Adv. Mater.* **2020**, *32*, 2003563.
[20] H. Wang, K. Wan, X. Shi, *Adv. Mater.* **2019**, *31*, 1805368.
[21] M. Liang, X. Yan, *Acc. Chem. Res.* **2019**, *52*, 2190.
[22] Q. Yang, J. Liu, W. Cai, X. Liang, Z. Zhuang, T. Liao, F. Zhang, W. Hu, P. Liu, S. Fan, W. Yu, B. Jiang, C. Li, D. Wang, Z. Xu, *Nano Lett.* **2023**, *23*, 8585.
[23] Q. Li, T. Wu, X. Fan, X. Guo, W. Jiang, K. Fan, *Mater. Des.* **2022**, *224*, 111430.
[24] X. Meng, D. Li, L. Chen, H. He, Q. Wang, C. Hong, J. He, X. Gao, Y. Yang, B. Jiang, G. Nie, X. Yan, L. Gao, K. Fan, *ACS Nano* **2021**, *15*, 5735.
[25] Z. Wang, X. Wang, X. Dai, T. Xu, X. Qian, M. Chang, Y. Chen, *Adv. Mater.* **2024**, *36*, 2312316.
[26] Y. Cheng, Y.-D. Xia, Y.-Q. Sun, Y. Wang, X.-B. Yin, *Adv. Mater.* **2024**, *36*, 2308033.
[27] M. Wang, M. Chang, Q. Chen, D. Wang, C. Li, Z. Hou, J. Lin, D. Jin, B. Xing, *Biomaterials* **2020**, *252*, 120093.
[28] T. Luo, H. Yang, R. Wang, Y. Pu, Z. Cai, Y. Zhao, Q. Bi, J. Lu, R. Jin, Y. Nie, X. Shuai, *ACS Nano* **2023**, *17*, 16715.
[29] P. Gong, H. Cui, C. Li, S. Song, Y. Gong, J. Li, B. Wang, F. Liu, D. Wang, Z. Liu, *Chem. Eng. J.* **2024**, *489*, 150941.
[30] A. Dhakshinamoorthy, S. Navalón, A. M. Asiri, H. Garcia, *ChemMedChem* **2020**, *15*, 2236.
[31] A. Dhakshinamoorthy, A. M. Asiri, H. Garcia, *Dalton Trans.* **2020**, *49*, 11059.
[32] B. Huang, J. Tian, Z. Cui, S. Weng, W. Wang, X. Jiang, W. Zhang, *Chem. Eng. J.* **2022**, *444*, 136164.
[33] D. Wang, H. Wu, S. Z. F. Phua, G. Yang, W. Qi Lim, L. Gu, C. Qian, H. Wang, Z. Guo, H. Chen, Y. Zhao, *Nat. Commun.* **2020**, *11*, 357.
[34] Z. Wang, Z. Li, Z. Sun, S. Wang, Z. Ali, S. Zhu, S. Liu, Q. Ren, F. Sheng, B. Wang, Y. Hou, *Sci. Adv.* **2020**, *6*, eabc8733.
[35] J. Chen, Q. Ma, M. Li, D. Chao, L. Huang, W. Wu, Y. Fang, S. Dong, *Nat. Commun.* **2021**, *12*, 3375.
[36] D. Feng, W. Chung, Z. Wei, Z. Gu, H. Jiang, Y. Chen, D. J. Darensbourg, H. Zhou, *J. Am. Chem. Soc.* **2013**, *135*, 17105.
[37] Y. Liu, Y. Cheng, H. Zhang, M. Zhou, Y. Yu, S. Lin, B. Jiang, X. Zhao, L. Miao, C. Wei, Q. Liu, Y. Lin, Y. Du, C. J. Butch, H. Wei, *Sci. Adv.* **2020**, *6*, eabb2695.
[38] D. Feng, Z.-Y. Gu, J.-R. Li, H.-L. Jiang, Z. Wei, H.-C. Zhou, *Angew. Chem., Int. Ed.* **2012**, *51*, 10307.
[39] N. Huang, S. Yuan, H. Drake, X. Yang, J. Pang, J. Qin, J. Li, Y. Zhang, Q. Wang, D. Jiang, H.-C. Zhou, *J. Am. Chem. Soc.* **2017**, *139*, 18590.
[40] F. Dosio, S. Arpicco, B. Stella, E. Fattal, *Adv. Drug Delivery Rev.* **2016**, *97*, 204.
[41] Z. Liu, W. Lin, Y. Liu, *Acc. Chem. Res.* **2022**, *55*, 3417.
[42] A. Lin, Q. Liu, Y. Zhang, Q. Wang, S. Li, B. Zhu, L. Miao, Y. Du, S. Zhao, H. Wei, *Anal. Chem.* **2022**, *94*, 10636.
[43] Q. Xu, G. Zhan, Z. Zhang, T. Yong, X. Yang, L. Gan, *Theranostics* **2021**, *11*, 1937.
[44] T. Mishchenko, I. Balalaeva, A. Gorokhova, M. Vedunova, D. V. Krysko, *Cell Death Dis.* **2022**, *13*, 455.
[45] R. Alzeibak, T. A. Mishchenko, N. Y. Shilyagina, I. V. Balalaeva, M. V. Vedunova, D. V. Krysko, *J. Immunother. Cancer* **2021**, *9*, e001926.
[46] C. Wang, Y. Guan, M. Lv, R. Zhang, Z. Guo, X. Wei, X. Du, J. Yang, T. Li, Y. Wan, X. Su, X. Huang, Z. Jiang, *Immunity* **2018**, *48*, 675.